Coastal Engineering 131 (2018) 42–50

Contents lists available at ScienceDirect

Coastal Engineering

journal homepage: www.elsevier.com/locate/coastaleng

Nonlinear and viscous effects on the hydrodynamic performance of a fixed OWC wave energy converter

Rong-quan Wang [a], De-zhi Ning [a,*], Chong-wei Zhang [a], Qing-ping Zou [b], Zhen Liu [c]

[a] State Key Laboratory of Coastal and Offshore Engineering, Dalian University of Technology, Dalian, 116024, China
[b] Department of Civil and Environmental Engineering, University of Maine, Orono, ME 04469, USA
[c] School of Naval Architecture and Ocean Engineering, Jiangsu University of Science and Technology, Zhenjiang, 212003, China

ARTICLE INFO

Keywords:
OWC
Wave energy converter
Hydrodynamic performance
Wave nonlinearity
Viscosity

ABSTRACT

The hydrodynamic performance of a fixed Oscillating Water Column (OWC) device is experimentally and numerically investigated. Based on the time-domain higher-order boundary element method (HOBEM), by introducing an artificial viscosity term in the dynamic free surface boundary condition, a fully nonlinear numerical wave model is used to simulate the hydrodynamic performance of an OWC device. A set of comprehensive experiments for regular waves is carried out to validate the numerical results as well as to investigate the nonlinear effects on the hydrodynamic performance of OWC. The mechanism of the nonlinear phenomenon is investigated based on the analysis of the experimental and numerical results. The influence of the wave nonlinearity and the viscosity on the hydrodynamic efficiency is quantified by comparing the linear and nonlinear numerical results. It was found that the hydrodynamic efficiency increases with the nonlinearity and viscosity when the incident wave amplitude is small. When the incident wave amplitude is large, the hydrodynamic efficiency is reduced by the weakened transmission of the second-order harmonic wave component due to the strong wave nonlinearity. However, when the wave amplitude is between these two regimes, the wave is weakly nonlinear, the efficiency decreases with the wave amplitude due to the combined effect of the nonlinearity and viscosity.

1. Introduction

Given its high power density, wave energy has the potential to become the lowest cost renewable energy source. In addition, it has the advantage of uninterrupted and continuous supply of energy over other renewable energy, such as wind and tidal energy. A wide variety of technologies are developed to harvest wave energy. OWC devices are believed to be one of the most popular wave energy converters (WECs) for viable wave energy harvesting. Yet the hydrodynamic performance of the OWC device remains not well-understood due to various factors, such as chamber geometry, wave nonlinear, water viscosity and power take-off damping. The influences of the nonlinearity and viscosity on the hydrodynamic performance are especially complex. The wave nonlinearity and viscosity are neglected in the theoretical study of the hydrodynamic performance of OWC devices (Evans, 1978, 1982; Falnes and McIver, 1985; McCormick, 1976) based on linear potential wave theory. Therefore, the hydrodynamic efficiency is often over-predicted.

Various nonlinear wave models have been developed to investigate the hydrodynamics of OWC (Elhanafi et al., 2016; Koo and Kim, 2010; Luo et al., 2014; Ning et al., 2015). It is found that hydrodynamic efficiency of the device is highly influenced by the incident wave amplitude for the given OWC geometrical parameters (Elhanafi et al., 2016; Luo et al., 2014; Ning et al., 2015, 2016). However, the influence of wave nonlinearity on OWC hydrodynamic efficiency is complex. The numerical simulations by Luo et al. (2014) suggest that the efficiency decreases with the wave amplitude. In contrast, the numerical and experimental studies by Ning et al. (2015, 2016) indicate that the hydrodynamic efficiency increases with wave amplitude first to a maximum value and deceases with wave amplitude thereafter. Through numerical study, Elhanafi et al. (2016) demonstrates that the hydrodynamic efficiency increases with the wave amplitude only when the damping factor is very small. However, there is a lack of understanding of the mechanism behind these phenomena. Luo et al. (2014) applied Fast Fourier Transform (FFT) to analyze the incident wave surface elevation and the transient air velocity at the outlet of the OWC. They attributed the decreased efficiency with wave amplitude to the energy transfers from the primary

* Corresponding author.
E-mail address: dzning@dlut.edu.cn (D.-z. Ning).

https://doi.org/10.1016/j.coastaleng.2017.10.012
Received 30 January 2017; Received in revised form 15 June 2017; Accepted 29 October 2017
Available online 7 November 2017

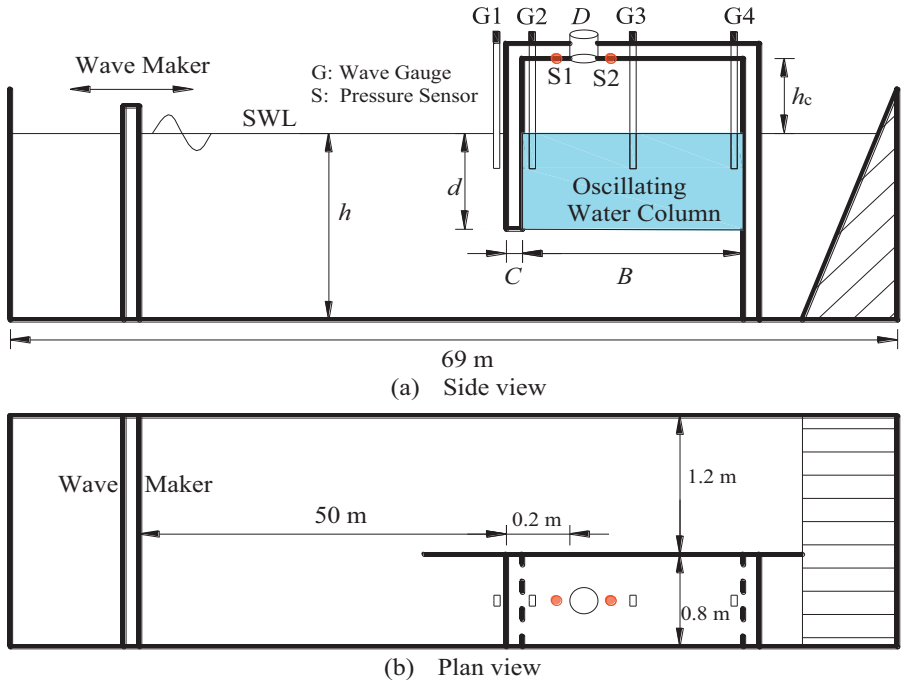

Fig. 1. Schematic of the experimental setup.

wave to the second-order wave component. However, the efficiency is more directly related to the inner surface motion than the incident wave surface. Therefore, it is worth to carry out a more systemic and comprehensive study of the influence of wave nonlinearity on the OWC efficiency.

Nonlinear wave interaction leads to energy transfer among different wave components at difference frequency. The wave dissipation is frequency dependent (Zou, 2004). Furthermore, the wave nonlinearity can produce local surface vortices (Filatov et al., 2016) which, of course, would also generated further energy dissipation. Accurately predicting the dissipation of gravity waves is a challenging problem due to wave nonlinearity, complex free surface deformation and evolution for steep and breaking wave (Bouscasse et al., 2014; Colagrossi et al., 2013, 2015; Iafrati et al., 2013; Lubin and Glockner, 2015; Wang et al., 2009). Energy loss occurs both at the entrance when incident waves enter the chamber and inside the chamber after wave generate an up-and-down motion of free surface within the chamber (He et al., 2016; Koo and Kim, 2010; Kuo et al., 2017; Müller and Whittaker, 1995; Tseng et al., 2000). Previous results of flow field suggest that the energy loss is affected by the wave conditions and the geometry of the front wall (Elhanafi et al., 2016; Fleming and Macfarlane, 2017; Kamath et al., 2015; López et al., 2015a; Teixeira et al., 2013; Vyzikas et al., 2017). Most of the OWC study that account for the energy loss due to the water viscosity were carried out using the Reynolds Averaged Navier-Stokes (RANS) equations (Elhanafi et al., 2016; Iturrioz et al., 2015; Kamath et al., 2015; López et al., 2014, 2016; Liu et al., 2016; Luo et al., 2014; Pereiras et al., 2015; Teixeira et al., 2013; Zhang et al., 2012). Babarit et al. (2012) and Iturrioz et al. (2014) introduce a friction force to take into account the viscous and turbulent losses at the chamber entrance by using Boundary Element Method (BEM). Additionally, the viscous effect may be incorporated by adding an artificial viscous damping term to the dynamic free surface boundary condition of the potential flow wave model (Koo and Kim, 2010; Ning et al., 2015). Although both these types of model have been shown to be in good agreement with the experimental data in the presence of viscosity (Wolgamot and Fitzgerald, 2015), it is not clear to what extent the viscosity would affect the hydrodynamic performance of OWC.

The main objective of this study is to elucidate the mechanism behind the nonlinear behavior in the OWC hydrodynamic performance. The influences of the wave nonlinearity and the viscosity on the hydrodynamic performance are investigated by comparing the linear and nonlinear numerical results. And the influence of the nonlinearity and the viscosity on the hydrodynamic efficiency is quantitative analyzed for the first time.

The rest of the present paper is organized as follows: The experimental procedure and numerical model are described in Section 2. In Section 3, the comparisons between the numerical results and experimental data are carried out firstly. Then, the nonlinear and viscous effects on the hydrodynamic performance of the OWC device are given in detail. Finally, the conclusions of this study are summarized in Section 4.

2. Model

2.1. Experimental model

The physical model tests were carried out in the wave-current flume at the State Key Laboratory of Coastal and Offshore Engineering, Dalian University of Technology, China. The wave-current flume is 69 m long, 2 m wide and 1.8 m high. It is equipped with a piston-type unidirectional wave maker that can generate regular and irregular waves with periods from 0.5 s to 5.0 s. The test section of the wave flume was divided into two parts along the longitudinal direction, which were 1.2 m and 0.8 m wide, respectively. The OWC model was installed at the part of 0.8 m wide and 50 m away from the wave maker (see Fig. 1). The OWC model was designed to span across the entire width and depth of the flume (i.e., the width of the flume $w = 0.8$ m). Fig. 1 shows the schematic of the experimental setup. The water depth h is 0.8 m, front wall thickness C is 0.04 m, chamber height h_c is 0.2 m, chamber width B is 0.55 m and front wall draft d is 0.14 m. The orifice was located on the ceiling of the chamber and was 0.2 m from the front wall. Note that it was not placed at the chamber center, due to the fact that there was a wave gauge fixed at the center of the ceiling. According to previous experimental studies (He and Huang, 2014; Ning et al., 2016), the optimal efficiency occurs at the opening ratio of $\alpha = S_0/S = 0.66\%$ (where S_0 and S are the cross-sectional areas of the orifice and the air-chamber ceiling, respectively). Thus, in the present study, the orifice diameter $D = 0.06$ m is chosen with the opening ratio $\alpha = 0.66\%$. Four wave gauges (i.e., G1 - G4) were used to

Table 1
Wave parameters used in the experiments.

T (s)	0.95	1.04	1.12	1.18	1.23	1.30	1.37	1.42	1.49	1.55	1.61	1.75	1.84	2.35
$A_i = 0.02$ m	–	–	–	–	–	–	✓	–	✓	–	✓	–	–	–
$A_i = 0.03$ m	✓	✓	✓	✓	✓	✓	✓	✓	✓	✓	✓	✓	✓	✓
$A_i = 0.04$ m	–	–	–	–	–	–	✓	–	✓	–	✓	–	–	–
$A_i = 0.05$ m	–	–	–	–	–	–	✓	–	✓	–	✓	–	–	–
$A_i = 0.06$ m	–	–	–	–	–	–	✓	–	✓	–	✓	–	–	–
$A_i = 0.07$ m	–	–	–	–	–	–	✓	–	✓	–	✓	–	–	–

measure the instantaneous surface elevation at different locations. Three of them (i.e., G2 - G4) were used to measure the surface elevation at different positions inside the chamber, and compare with each other to ensure the reliability of the measurements and provide more data to validate the numerical model. Two pressure sensors (S1 and S2) were used to record the air pressure inside the chamber. Their average is regarded as the air pressure in the chamber.

In the experiments, 6 wave amplitudes A_i (0.02 m–0.07 m) and 14 wave periods T (0.95 s–2.35 s) were used. The incident wave parameters were recorded by performing a test of wave propagation in the wave flume without the OWC model, and the wave parameters at the position where the OWC model was to be fixed were measured. The present study focuses on regular waves for simplicity of analysis of model results. The detailed wave parameters are given in Table 1.

There are three steps in the process of the wave energy transfer to the electrical energy (1) the OWC chamber converts the wave energy into the kinetic energy of the air flow; (2) the turbine converts the air flow kinetic energy into mechanical energy of the rotor; and (3) the generator converts the mechanical energy into electrical energy, respectively. In the present study, only the first transfer step from wave energy to air flow energy is considered. Thus, losses due to friction through the top orifice are not considered. The water motion in the chamber can be well represented by that at the chamber-center under the long waves. For the cases under short waves, there are some errors associated this representation. Short wave is away from the resonant frequency, therefore, not the focus of wave energy harness. Then, the wave power absorbed by the wave energy device (i.e., P_{owc}) can be calculated from the observed air pressure and surface elevation at chamber center by wave gauge G3 (Morris-Thomas et al., 2007; Ning et al., 2016), and is written as follows:

$$P_{owc} = \int_{S_f} P_a(t)\cdot\dot{\eta}(t)\mathrm{dS} = \frac{Bw}{T}\int_t^{t+T} P_a(t)\cdot\dot{\eta}(t)\mathrm{d}t, \tag{1}$$

where p_a is the air pressure in the chamber, η is the vertical elevation of the free surface inside the chamber (approximated by that at the chamber center) and $\dot{\eta}$ is the time rate of change of η and the vertical velocity of the free surface, S_f is the cross-section area of the free surface in the chamber, w is the width of the flume and T is the wave period.

From linear wave theory, the average energy flux per unit width in the incident wave (i.e., P_{inc}) is

$$P_{inc} = \frac{\rho g A_i^2 \omega}{4k}\left(1 + \frac{2kh}{\sinh kh}\right), \tag{2}$$

where ρ is the water density, g is the gravitational acceleration, A_i is the incident wave amplitude, ω is the angular frequency and k is the wave number which is determined according to the dispersion relationship $\omega^2 = gk\tanh(kh)$.

Thus, the hydrodynamic efficiency becomes

$$\xi = \frac{P_{owc}}{P_{inc}\cdot w}. \tag{3}$$

2.2. Numerical model

To simulate the hydrodynamic performance of a land-fixed OWC, we use the two-dimensional (2-D) fully nonlinear numerical wave flume based on the potential theory and time-domain higher-order boundary element method (HOBEM) developed by Ning et al. (2015). This numerical model has been successfully validated against analytical solutions (Evans and Porter, 1995), numerical results (Zhang et al., 2012) and experimental data (Morris-Thomas et al., 2007). In the numerical wave flume, a Cartesian coordinate system Oxz is chosen with its origin on the still water level, and the z-axis pointing upward. The incident waves are generated using the inner sources in the computational domain to avoid the reflection of the reflected waves from the OWC device at the wave maker. The source strength is directly controlled by the horizontal fluid speed (corresponding to the wave to be generated), which is given as the second-order Stokes analytical solution in the present study. The governing equation is described with Poisson equation. The detailed information can be found in Ning et al. (2015).

In this study, a sponge layer with a damping coefficient $\mu_1(x)$ at the inlet of the numerical flume is applied to absorb the reflected waves from the OWC device. An artificial viscous damping term with a damping coefficient μ_2 is applied to the dynamic free surface boundary condition inside the OWC chamber to account for the energy loss due to vortex shedding and flow separation, etc. Thus, the fully nonlinear free surface boundary conditions are given as:

$$\begin{cases} \dfrac{d\vec{X}(x,z)}{\mathrm{d}t} = \nabla\phi - \mu(x)\left(\vec{X} - \vec{X}_0\right) \\ \dfrac{\mathrm{d}\phi}{\mathrm{d}t} = -g\eta - \dfrac{p_a}{\rho} - \mu_1(x)\phi + (N-1)\dfrac{1}{2}|\nabla\phi|^2 - (M-1)\mu_2\dfrac{\partial\phi}{\partial n} \end{cases}, \tag{4}$$

where $\vec{X}(x,z)$ denotes the position vector of a fluid particle on the free surface and $\vec{X}_0 = (x_0, 0)$ the initial static position of the fluid particle, ϕ the velocity potential, t the time, n the outward normal vector. N and M are the control weight coefficient of the quadratic term and viscous term, respectively. Both are assigned a value of 1 or 2 (i.e., $N = M = 2$), nonlinear model with artificial viscous term (NL.V.); $N = M = 1$, linear model without artificial viscus term (L.NV.). The material derivative is defined as $\mathrm{d}/\mathrm{d}t = \partial\phi/\partial t + \nabla\phi\cdot\nabla$. The damping coefficient $\mu_1(x)$ is defined by

$$\mu_1(x) = \begin{cases} \omega\left(\dfrac{x - x_1}{L_d}\right)^2, & x_1 - L_d < x < x_1 \\ 0, & x \geq x_1 \end{cases}, \tag{5}$$

where x_1 is the starting position of sponge layer, L_d is the length of the sponge layer given to be 1.5 times the incident wavelength (i.e., 1.5L, where L is the wavelength) in the present study. The value of the artificial viscous damping coefficient μ_2 is determined by trial and error method by comparison with the experimental data. The detailed process can be found in Appendix B in Ning et al. (2016). μ_2 is only implemented inside the chamber.

Outside of the chamber, the air pressure p_a on the free surface is set to be zero (i.e., atmospheric pressure), while inside the chamber, the pneumatic pressure is specified on the free-surface:

$$P_a(t) = C_{dm}U_d(t), \tag{6}$$

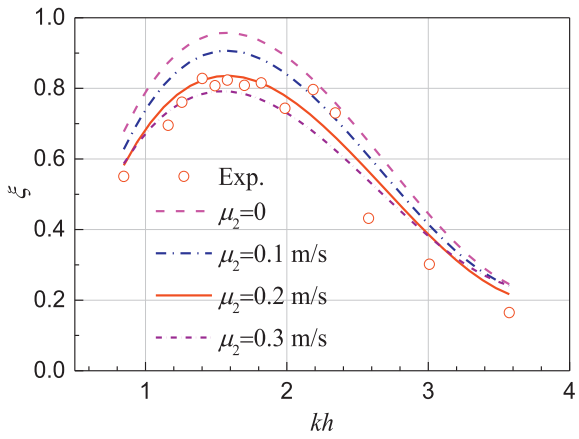

Fig. 2. The predicted hydrodynamic efficiency with a damping coefficient $\mu_2 = 0$, 0.1, 0.2, 0.3 m/s for a constant incident wave amplitude of $A_i = 0.03$ m.

where C_{dm} is the linear pneumatic damping coefficient and U_d the air flow velocity through the orifice. We assume that the air compressibility can be ignored within the air chamber (Elhanafi et al., 2017a, 2017b). Based on the incompressibility assumption of the air inside the chamber, the air flow velocity U_d can be expressed as follows:

$$U_d(t) = \frac{\Delta V}{S_0 \Delta t}, \tag{7}$$

where $\Delta V = V_{t+\Delta t} - V_t$ represents the change of air volume in the chamber within each time step Δt. S_0 is the cross-sectional area of the air orifice.

All simulations start with the initial state

$$\phi|_{t=0} = \eta|_{t=0} = 0. \tag{8}$$

In the numerical simulations, the length of the numerical wave flume is 5L, in which 1.5L at the left side is used as the sponge layer. In all cases, there are 30 mesh segments per wave length on the free surface, 15 mesh segments are distributed on the front wall surface, and 10 mesh segments are used across the depth of the numerical wave flume. For each case, 30 wave periods are simulated with a time step of $\Delta t = T/80$.

3. Results and discussion

3.1. Nonlinearity and viscosity

Fig. 2 shows the comparison of the model predictions of hydrodynamic efficiency for different viscous coefficient μ_2 with the measurements for a constant incident wave amplitude $A_i = 0.03$ m. The normalized error between the predicted and measured wave power $\sigma = |P_{owc(Exp.)} - P_{owc(Num.)}|/P_{owc(Exp.)max}$, where $P_{owc(Exp.)}$ is the measured wave power, $P_{owc(Exp.)max}$ the maximum value of the measured wave power and $P_{owc(Num.)}$ the predicted wave power absorbed by the OWC device, is shown in Table 2. It is evident from Fig. 2 and Table 2 that the numerical model can capture the observed hydrodynamic performance of the OWC well by adjusting the value of μ_2. Under the given wave condition (i.e., $A_i = 0.03$ m) and chamber geometry, $\mu_2 = 0.2$ m/s is chosen in the following based on the results both in Fig. 2 and Table 2. Though the discrepancies are large for high frequency waves (i.e., short waves) in Fig. 2, which may due to spatial variation of the surface elevation in the chamber, the numerical results show good agreement with experimental data near the resonant frequency (region of $kh = 1$–2) which is the parameter regime we focus on in this study. To further check the rationality of the value of chosen viscous coefficient (i.e., $\mu_2 = 0.2$), the comparisons of the time series of surface elevation at four measured points and air pressure in the chamber with wave periods of $T = 1.49$ s and $T = 1.55$ s are carried out, as shown in Figs. 3 and 4, respectively. From the figures, it can be observed that the numerical and experimental results compare well with each other. It is evident from Figs. 3 (a) and (b), the wave tilts backwards especially at gauge 1 signifying the

Table 2
The normalized error between the predicted and measured results.

T (s)	0.95	1.04	1.12	1.18	1.23	1.30	1.37	1.42	1.49	1.55	1.61	1.75	1.84	2.35	RMSE
kh	3.57	3.01	2.58	2.34	2.19	1.99	1.82	1.70	1.58	1.49	1.40	1.26	1.16	0.85	
$\mu_2 = 0$	0.10	0.19	0.23	0.00	0.10	0.20	0.16	0.18	0.16	0.14	0.12	0.25	0.18	0.16	0.060
$\mu_2 = 0.1$ (m/s)	0.09	0.16	0.18	0.04	0.01	0.15	0.10	0.12	0.10	0.10	0.06	0.14	0.14	0.10	0.046
$\mu_2 = 0.2$ (m/s)	0.06	0.11	0.14	0.09	0.10	0.05	0.04	0.04	0.02	0.03	0.01	0.01	0.06	0.06	0.038
$\mu_2 = 0.3$ (m/s)	0.09	0.11	0.12	0.14	0.14	0.02	0.06	0.03	0.03	0.02	0.05	0.01	0.04	0.04	0.045

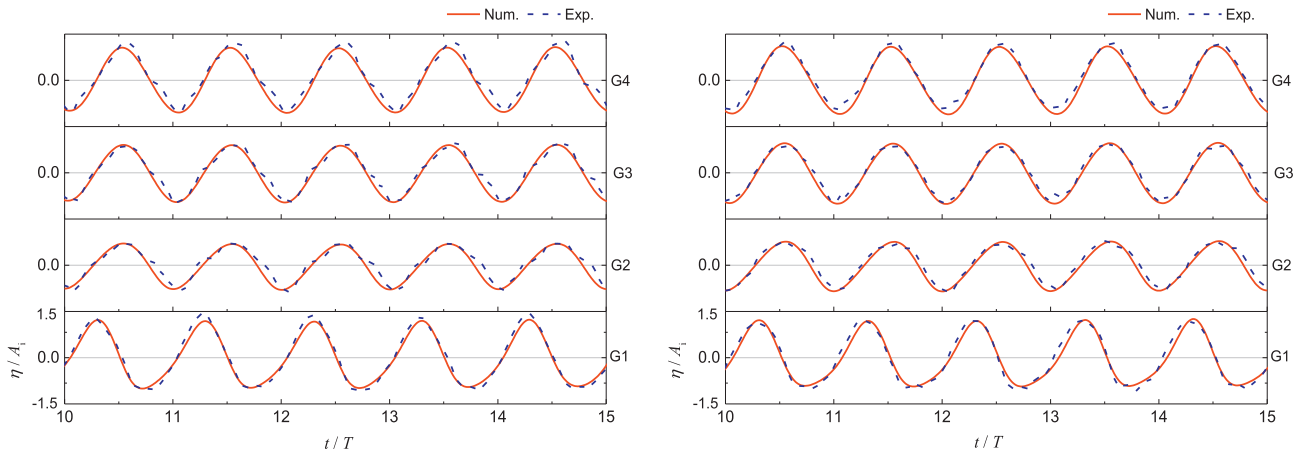

Fig. 3. Time series of the predicted (solid line) and measured (dashed line) surface elevation at the four gauge positions for wave periods $T = 1.49$ s and 1.55 s ($A_i = 0.03$ m).

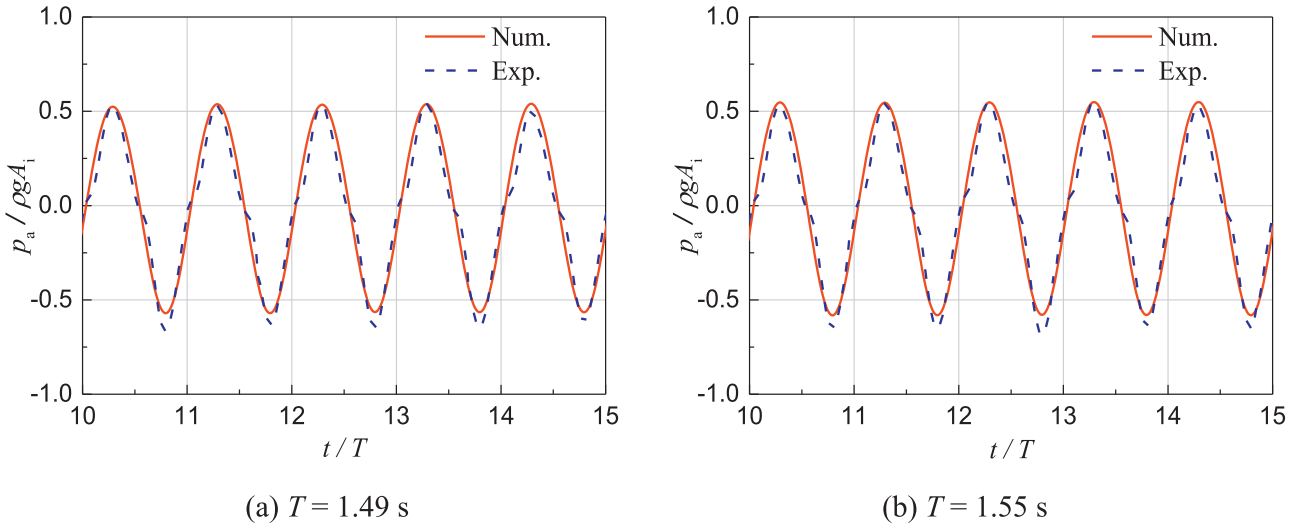

Fig. 4. Time series of the predicted (solid line) and measured (dashed line) air pressure in the chamber for wave periods $T = 1.49$ s and 1.55 s ($A_i = 0.03$ m).

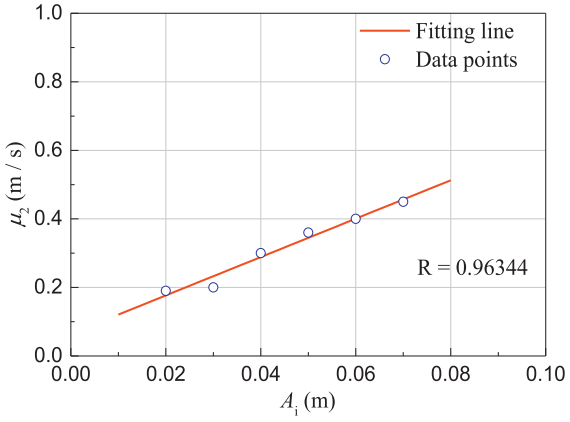

Fig. 5. Values of artificial viscous coefficient μ_2 in different wave conditions.

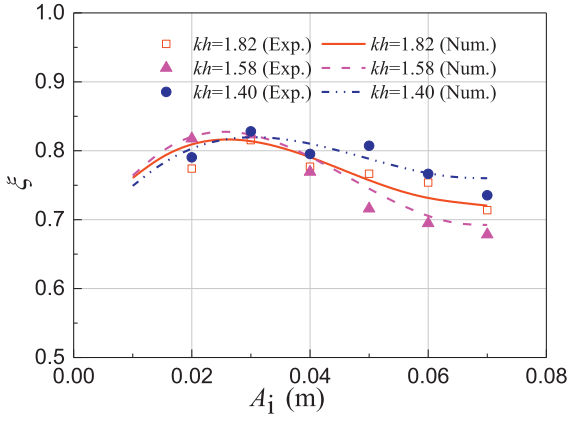

Fig. 6. Variation of the hydrodynamic efficiency with incident wave amplitude when $kh = 1.40$ (i.e., $T = 1.60$ s), 1.58 (i.e., $T = 1.49$ s) and 1.82 (i.e., $T = 1.37$ s), respectively.

increased wave asymmetry arising from self-self and sum nonlinear wave interactions due to wave structure interaction and enhanced wave nonlinearity (Elgar et al., 1990; Peng et al., 2009; Zou and Peng, 2011).

The values of μ_2 in other wave conditions are determined using the same method. The chamber geometry in the present study are fixed and the influence of the wave period on the viscous is considered through the

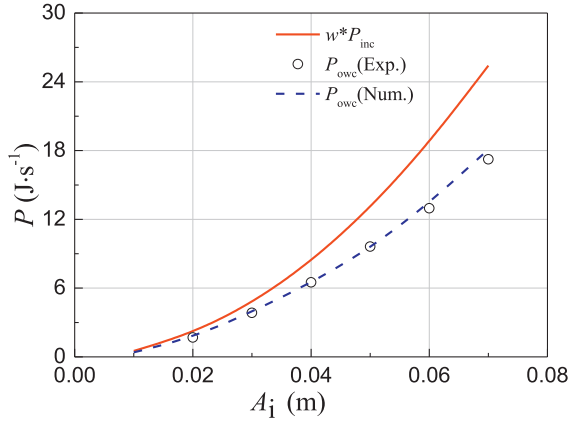

Fig. 7. Variation of wave power absorbed by the OWC (dashed line) and the incident wave power (solid line) with the incident wave amplitudes for a constant $kh = 1.58$ (i.e, $T = 1.49$ s).

viscous term $\frac{\partial \phi}{\partial n}$. Thus, μ_2 is assumed to be a function of the wave amplitude. Its optimum values for different wave conditions and their linear fitting line are shown in Fig. 5. A good linear correlation between the incident wave amplitude and artificial viscous coefficient is observed (coefficient of determination R = 0.96344). The equation of the linear fit is

$$\mu_2 = 5.6A_i + 0.06467. \quad (9)$$

Fig. 6 shows the variation of the model predicted hydrodynamic efficiency with incident wave amplitude in comparison with the measurement when $kh = 1.40$, 1.58 and 1.82, respectively. Fig. 7 shows the variation of the wave power absorbed by the OWC and incident wave power with incident wave amplitudes at $kh = 1.58$. It shows the good agreement between the numerical model and experiment. The hydrodynamic efficiency first increases with increasing wave amplitude when the wave amplitude is small therefore wave nonlinearity is weak, and then decreases with the wave amplitude after the wave amplitude reaches a certain value. A similar phenomenon was observed by López et al. (2015b) in their experimental study of OWC device. This is due to the fact that the growth rate of wave power absorbed by the OWC with wave amplitude is lower than that of the incident wave power as shown in Fig. 7.

To further investigate the contribution of wave nonlinearity to the

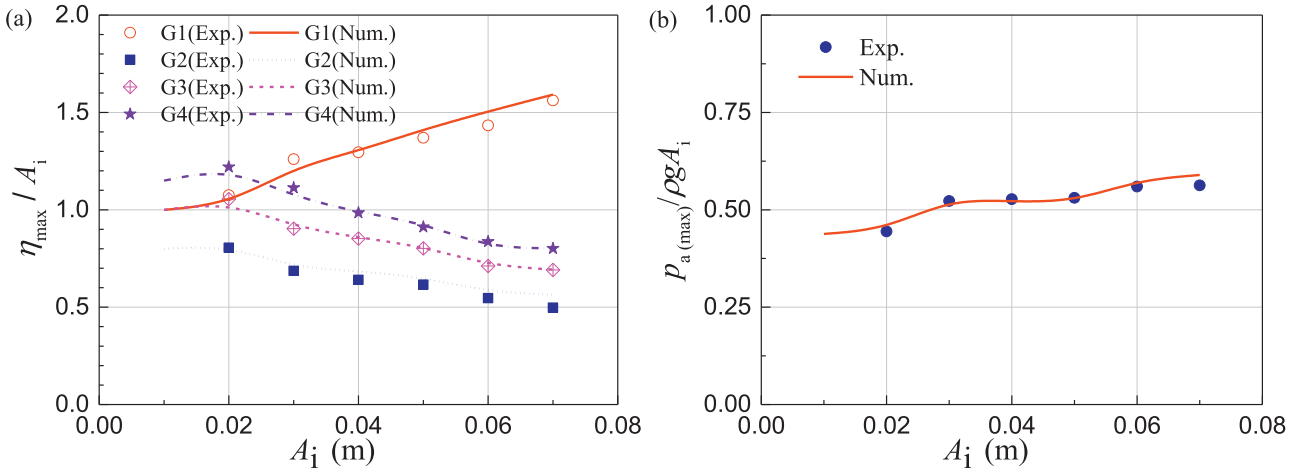

Fig. 8. Variation of (a) surface elevation at 4 wave gauge locations G1 - G4 and (b) air pressure in chamber with incident wave amplitudes ($T = 1.49$ s, $kh = 1.58$).

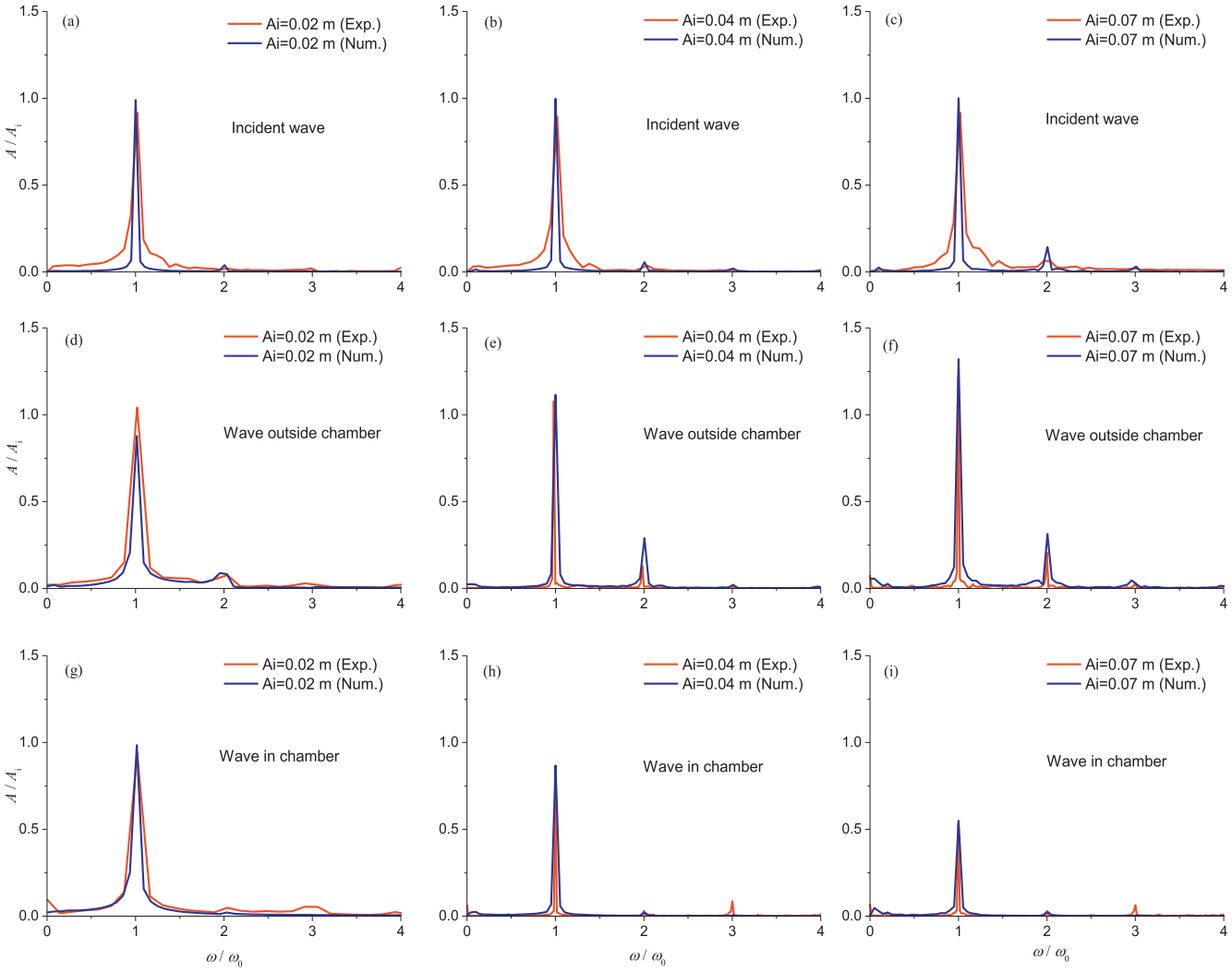

Fig. 9. Amplitude spectra of incident wave free surface elevation for (a) $A_i = 0.02$ m, (b) $A_i = 0.04$ m and (c) $A_i = 0.07$ m; amplitude spectra of surface elevation at gauge G1 outside the chamber for (d) $A_i = 0.02$ m, (e) $A_i = 0.04$ m and (f) $A_i = 0.07$ m; amplitude spectra of surface elevation at gauge G3 inside the chamber (g) $A_i = 0.02$ m, (h) $A_i = 0.04$ m and (i) $A_i = 0.07$ m (see gauge locations indicated by Fig. 1) ($T = 1.49$ s, i.e., $kh = 1.58$ for all the cases).

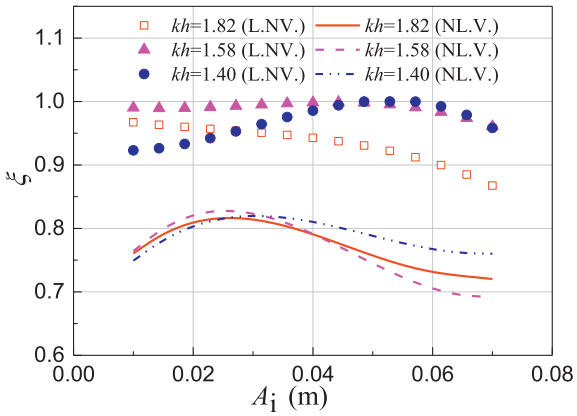

Fig. 10. Effects of the wave nonlinear and viscous term on the hydrodynamic efficiency.

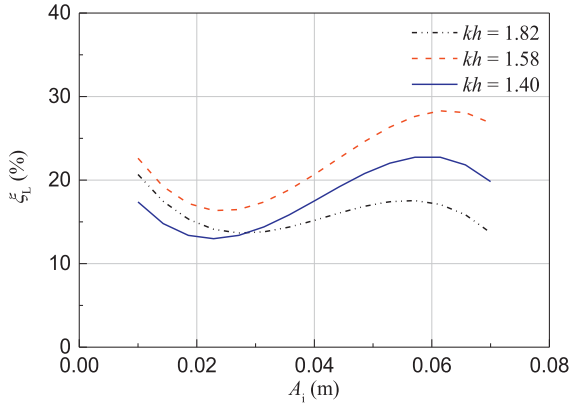

Fig. 11. Reduction of hydrodynamics efficiency due to wave nonlinearity and viscous effect for different wave frequency *kh*.

OWC efficiency, we firstly analyze the relationship between the dimensionless surface elevation both inside and outside the chamber as well as that between the dimensionless air pressure in the chamber and the incident wave amplitudes. According to Eq. (1), the wave power absorbed by OWC is determined by both the surface elevation and the air pressure in the chamber. We assume that the relation between the surface motion and the air pressure in the chamber is linear and that there is a phase lag of π/2 between the surface elevation and the pressure (Wang et al., 2002; Zhang et al., 2012). This is easy to understand, according to Eqs. (6) and (7), the air pressure is in phase with the air flow velocity which is in phase with the velocity of the surface elevation inside the chamber. The phase difference between the surface displacement and velocity of surface elevation is π/2. Thus, there is a phase lag of π/2 between the surface elevation and the air pressure inside the chamber. Then, Eq. (3) of efficiency can be approximated by:

$$\xi = \frac{\frac{BwP_{a(\max)}\eta_{\max}\omega}{2}}{\frac{\rho g\omega A_i^2}{4k}\left(1+\frac{2kh}{\sinh kh}\right)\cdot w} \sim \frac{\eta_{\max}}{A_i}\cdot\frac{P_{a(\max)}}{\rho g A_i}. \tag{10}$$

The efficiency is proportional to the dimensionless surface elevation and air pressure in the chamber according to Eq. (10). From the numerical results shown in Fig. 8 (a), it can be seen that the dimensionless surface elevation $\eta_{\max}/A_i$ inside the chamber (G2 - G4) decreases with increasing incident amplitude after a slight increase when the wave amplitude is smaller than 0.02 (i.e., wave nonlinearity is weak), while the dimensionless surface $\eta_{\max}/A_i$ outside the chamber (G1) increases continuously with the incident amplitude. In addition, it can be seen that the surface elevation amplitude of the three wave gauges inside the chamber (i.e., G2 - G4) is not the same, which is due to the spatial variation of free surface inside the chamber. The amplitude of G3 is close to the average amplitude of G2 and G4. This further justify that G3 can be used to represent the surface elevation inside the chamber. The value of dimensionless air pressure $P_{a(\max)}/\rho g A_i$ in the chamber, which is induced by the motion of the water column, is close to 0.5 and increases slightly with increasing wave amplitude as illustrated in Fig. 8 (b). Because of the decreasing rate of the dimensionless surface elevation is much larger than the increasing rate of the dimensionless air pressure when the incident wave amplitude A_i is greater than the critical wave amplitude, which is close to 0.03 m under the given geometry, the efficiency shows a declining trend with increasing A_i. However, when $A_i < 0.02$ m (i.e., the wave nonlinearity is weak), both the dimensionless air pressure and surface elevation in the chamber increases with A_i. For $0.02\text{ m} < A_i < 0.03$ m, the increasing rate of dimensionless air pressure is larger than the decreasing rate of dimensionless surface elevation in the chamber. As a result, the efficiency increases with A_i before the incident wave amplitude reaches the critical value of 0.03 m as shown in Fig. 6.

Next, we will apply spectral analysis to the incident wave, the surface elevation inside the chamber and outside the chamber at G1 and G3 for wave amplitudes $A_i = 0.02$, 0.06 and 0.07 m. Fig. 9 (a), (b) and (c) show three incident waves with different amplitudes. The primary wave components for all these three waves are similar, while the second-order components at harmonic frequency increase with incident amplitude. The surface elevation spectra change dramatically once the wave acts with the chamber. As shown in Fig. 9 (d), (e) and (f), while the second-order harmonic component of the wave surface is significant outside the chamber at gauge G1, it is negligible inside the chamber at gauge G3 as shown in Fig. 9 (g), (h) and (i). Furthermore, the proportion of wave energy contained within the second-order harmonic wave component outside the chamber increases with incident wave amplitude. Namely, the second-order components of the incident wave increase with wave nonlinearity, but it is suppressed once it enters the chamber due to weaker transmission at the second-order harmonic frequency. As the wave approach the OWC device, wave energy is transferred from the first-order primary wave to the second-order harmonic waves. This explains why the surface elevation outside the chamber increases and that inside the chamber decreases with increasing wave amplitude when the wave nonlinearity is strong.

3.2. Energy loss

The effects of nonlinearity and viscosity on the hydrodynamic efficiency are shown in Fig. 10. Both the numerical results with the nonlinear and viscous term (nonlinear model with artificial viscous term (NL.V.), i.e., $N = M = 2$) and without the nonlinear and viscous term (linear model without artificial viscous term (L.NV.), i.e., $N = M = 1$) are shown in Fig. 10. Note that, the nonlinear viscous model results show a good agreement with the experimental data as indicated in Fig. 6. The experimental data is not shown in this figure again. It is evident that the influence of the nonlinearity on the hydrodynamic efficiency is dependent on the wave frequency. The model predicted the largest efficiency, which is close to 1 when the nonlinearity is weak, at the resonant frequency $kh = 1.58$. The L.NV. efficiency decreases with the incident wave amplitude increasing when the frequency is higher than the resonant frequency, i.e., $kh = 1.82$.

To quantify the effect of the nonlinearity and viscosity on the hydrodynamic efficiency, we calculate the energy loss using the numerical model by taking $N = M$ as 1 or 2. The reduction in hydrodynamic efficiency due to the nonlinearity and viscous effect is given by:

$$\xi_L = \frac{P_{owc(1)} - P_{owc(2)}}{w\cdot P_{inc}} \times 100\%, \tag{11}$$

where $P_{owc(1)}$ and $P_{owc(2)}$ represent the absorbed power predicted by the numerical model at $N = M = 1$ and $N = M = 2$, respectively. Due to the

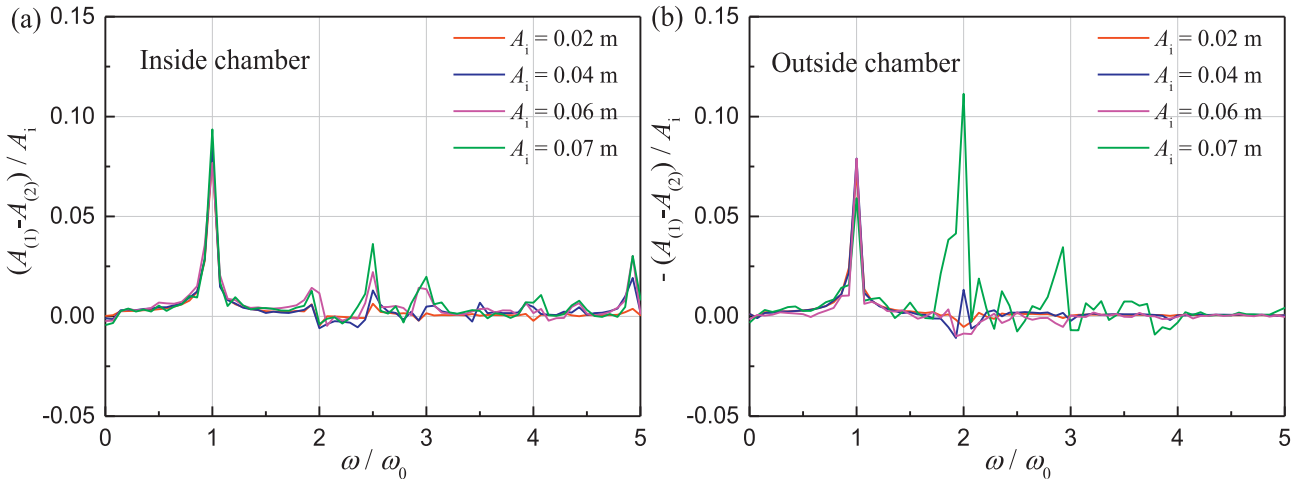

Fig. 12. The difference between the surface elevation spectra predicted by the linear no viscous model and nonlinear viscous model at $kh = 1.58$ (i.e., $T = 1.49$ s) for incident wave amplitude $A_i = 0.02$, 0.04, 0.06 and 0.07 m at (a) gauge G3 (i.e., inside chamber); (b) G1 (i.e., outside chamber). $A_{(1)}$ and $A_{(2)}$ represent the amplitude of the surface elevation predicted by the numerical model using $N = M = 1$ and $N = M = 2$, respectively.

fact that the numerical model can predict the efficiency well when $N = M = 2$, we assume that $P_{owc(2)}$ represents the real power absorbed by the device. And then, the energy losses can be predicted by Eq. (11). The variation of energy loss with the incident wave amplitude for different kh is plotted in Fig. 11. It shows that the largest energy loss occurs at resonant frequency $kh = 1.58$ and it reduce the advantage of OWC operation at the resonant frequency (Wolgamot and Fitzgerald, 2015). The efficiency loss due to nonlinearity and viscous effect decrease with wave amplitude for small wave of $A_i < 0.02$ m and increase with wave amplitude for larger waves for 0.02 m $< A_i <$ 0.06 m and decrease again for even larger waves with an amplitude $A_i > 0.06$ m. This also illustrates that the efficiency increases with amplitude when the wave nonlinearity is weak.

There is also a drop in the efficiency loss when the nonlinearity is very strong when $A_i > 0.06$ m. To explain this phenomenon, the difference between the free surface elevation spectra predicted by linear and nonlinear model at resonant frequency $kh = 1.58$ for a range of incident wave amplitude is plotted in Fig. 12. The surface elevation spectrum at gauge G3 is very similar for different wave amplitude. Although the difference in the first order primary wave component at gauge G1 outside the chamber are also similar, that in the second-order harmonic wave component is very large when $A_i = 0.07$ m because it is reflected by the front wall and unable to transmit into the chamber. These results suggest that when wave amplitude increases (i.e., the nonlinearity becomes very strong), the effect of the second-order harmonic wave component on the efficiency is enhanced while the viscous effect on the efficiency is weakened gradually. We may draw the conclusion that the weak transmission of the second-order component wave energy into the chamber cause the efficiency to decrease when the nonlinearity is strong.

4. Conclusion

In conclusion, we have provided insight into how and why wave nonlinearity and viscosity may affect the operation of the OWC device. We evaluated, for the first time to our knowledge, the degree of the influence of the viscosity and nonlinearity on the hydrodynamic efficiency by comparisons of numerical model results with and without the nonlinear and viscous term. We demonstrated that the efficiency is increased by the nonlinearity and viscosity when the incident wave amplitude is very small. When the incident wave amplitude is very large, the efficiency is decreased mainly by the weakened transmission of the second-order harmonic wave component due to the strong nonlinearity. However, when the wave amplitude is between these two regimes and wave is weakly nonlinear, the efficiency decreases with wave amplitude due to the combined effect of the nonlinearity and viscosity. Our analysis method can be extended to apply to other kinds of wave energy converters and marine structures. The results of our experimental and numerical studies allow one to better understand the influence of the nonlinearity and viscosity on the hydrodynamic efficiency.

Acknowledgements

This study is financially supported by the National Science Foundation of China (Grant Nos. 51679036, 51490672), the Royal Academy of Engineering under the UK-China Industry Academia Partnership Programme (Grant No.UK-CIAPP\73) and the Fundamental Research Funds for the Central Universities.

References

Babarit, A., et al., 2012. Numerical benchmarking study of a selection of wave energy converters. Renew. Energy 41, 44–63.
Bouscasse, B., Colagrossi, A., Souto-Iglesias, A., Cercos-Pita, J.L., 2014. Mechanical energy dissipation induced by sloshing and wave breaking in a fully coupled angular motion system. Ii. Experimental investigation. Phys. Fluids 26 (3), 033104.
Colagrossi, A., Bouscasse, B., Marrone, S., 2015. Energy-decomposition analysis for viscous free-surface flows. Phys. Rev. E Stat. Nonlin Soft Matter Phys. 92 (5), 053003.
Colagrossi, A., Souto-Iglesias, A., Antuono, M., Marrone, S., 2013. Smoothed-particle-hydrodynamics modeling of dissipation mechanisms in gravity waves. Phys. Rev. E Stat. Nonlin Soft Matter Phys. 87 (2), 023302.
Elgar, S., Freilich, M.H., Guza, R.T., 1990. Model-data comparisons of moments of nonbreaking shoaling surface gravity waves. J. Geophys. Res. 95 (C9), 16055.
Elhanafi, A., Fleming, A., Macfarlane, G., Leong, Z., 2016. Numerical energy balance analysis for an onshore oscillating water column-wave energy converter. Energy 116, 539–557.
Elhanafi, A., Macfarlane, G., Fleming, A., Leong, Z., 2017a. Investigations on 3d effects and correlation between wave height and lip submergence of an offshore stationary owc wave energy converter. Appl. Ocean Res. 64, 203–216.
Elhanafi, A., Macfarlane, G., Fleming, A., Leong, Z., 2017b. Scaling and air compressibility effects on a three-dimensional offshore stationary owc wave energy converter. Appl. Energy 189, 1–20.
Evans, D., 1978. The oscillating water column wave-energy device. IMA J. Appl. Math. 22 (4), 423–433.
Evans, D., 1982. Wave-power absorption by systems of oscillating surface pressure distributions. J. fluid Mech. 114 (1), 481–499.
Evans, D., Porter, R., 1995. Hydrodynamic characteristics of an oscillating water column device. Appl. Ocean Res. 17 (3), 155–164.
Falnes, J., McIver, P., 1985. Surface wave interactions with systems of oscillating bodies and pressure distributions. Appl. Ocean Res. 7 (4), 225–234.
Filatov, S.V., et al., 2016. Nonlinear generation of vorticity by surface waves. Phys. Rev. Lett. 116 (5), 054501.
Fleming, A.N., Macfarlane, G.J., 2017. Experimental flow field comparison for a series of scale model oscillating water column wave energy converters. Mar. Struct. 52, 108–125.
He, F., Huang, Z., 2014. Hydrodynamic performance of pile-supported owc-type structures as breakwaters: an experimental study. Ocean. Eng. 88, 618–626.

He, F., Li, M., Huang, Z., 2016. An experimental study of pile-supported owc-type breakwaters: energy extraction and vortex-induced energy loss. Energies 9 (7).
Iafrati, A., Babanin, A., Onorato, M., 2013. Modulational instability, wave breaking, and formation of large-scale dipoles in the atmosphere. Phys. Rev. Lett. 110 (18), 184504.
Iturrioz, A., et al., 2014. Time-domain modeling of a fixed detached oscillating water column towards a floating multi-chamber device. Ocean. Eng. 76, 65–74.
Iturrioz, A., Guanche, R., Lara, J.L., Vidal, C., Losada, I.J., 2015. Validation of openfoam® for oscillating water column three-dimensional modeling. Ocean. Eng. 107, 222–236.
Kamath, A., Bihs, H., Arntsen, Ø.A., 2015. Numerical investigations of the hydrodynamics of an oscillating water column device. Ocean. Eng. 102, 40–50.
Koo, W., Kim, M.-H., 2010. Nonlinear time-domain simulation of a land-based oscillating water column. Journal of Waterway. Port, Coast. Ocean Eng. 136 (5), 276–285.
Kuo, Y.-S., Chung, C.-Y., Hsiao, S.-C., Wang, Y.-K., 2017. Hydrodynamic characteristics of oscillating water column caisson breakwaters. Renew. Energy 103, 439–447.
López, I., Castro, A., Iglesias, G., 2015a. Hydrodynamic performance of an oscillating water column wave energy converter by means of particle imaging velocimetry. Energy 83, 89–103.
López, I., Pereiras, B., Castro, F., Iglesias, G., 2014. Optimisation of turbine-induced damping for an owc wave energy converter using a rans–vof numerical model. Appl. Energy 127, 105–114.
López, I., Pereiras, B., Castro, F., Iglesias, G., 2015b. Performance of owc wave energy converters: influence of turbine damping and tidal variability. Int. J. Energy Res. 39 (4), 472–483.
López, I., Pereiras, B., Castro, F., Iglesias, G., 2016. Holistic performance analysis and turbine-induced damping for an owc wave energy converter. Renew. Energy 85, 1155–1163.
Liu, Z., Hyun, B., Jin, J., Hong, K., Lee, Y., 2016. Owc air chamber performance prediction under impulse turbine damping effects. Sci. China Technol. Sci. 59 (4), 657–666.
Lubin, P., Glockner, S., 2015. Numerical simulations of three-dimensional plunging breaking waves: generation and evolution of aerated vortex filaments. J. Fluid Mech. 767, 364–393.
Luo, Y., Nader, J.-R., Cooper, P., Zhu, S.-P., 2014. Nonlinear 2d analysis of the efficiency of fixed oscillating water column wave energy converters. Renew. Energy 64, 255–265.
Müller, G., Whittaker, T.J.T., 1995. Visualisation of flow conditions inside a shoreline wave power-station. Ocean. Eng. 22 (6), 629–641.
McCormick, M.E., 1976. A modified linear analysis of a wave-energy conversion buoy. Ocean. Eng. 3 (3), 133–144.
Morris-Thomas, M.T., Irvin, R.J., Thiagarajan, K.P., 2007. An investigation into the hydrodynamic efficiency of an oscillating water column. J. Offshore Mech. Arct. Eng. 129 (4), 273–278.
Ning, D.-Z., Shi, J., Zou, Q.-P., Teng, B., 2015. Investigation of hydrodynamic performance of an owc (oscillating water column) wave energy device using a fully nonlinear hobem (higher-order boundary element method). Energy 83, 177–188.
Ning, D.-Z., Wang, R.-Q., Zou, Q.-P., Teng, B., 2016. An experimental investigation of hydrodynamics of a fixed owc wave energy converter. Appl. Energy 168, 636–648.
Peng, Z., Zou, Q., Reeve, D., Wang, B., 2009. Parameterisation and transformation of wave asymmetries over a low-crested breakwater. Coast. Eng. 56 (11–12), 1123–1132.
Pereiras, B., López, I., Castro, F., Iglesias, G., 2015. Non-dimensional analysis for matching an impulse turbine to an owc (oscillating water column) with an optimum energy transfer. Energy 87, 481–489.
Teixeira, P.R.F., Davyt, D.P., Didier, E., Ramalhais, R., 2013. Numerical simulation of an oscillating water column device using a code based on navier–stokes equations. Energy 61, 513–530.
Tseng, R.-S., Wu, R.-H., Huang, C.-C., 2000. Model study of a shoreline wave-power system. Ocean. Eng. 27 (8), 801–821.
Vyzikas, T., Deshoulières, S., Giroux, O., Barton, M., Greaves, D., 2017. Numerical study of fixed oscillating water column with rans-type two-phase cfd model. Renew. Energy 102, 294–305.
Wang, D.J., Katory, M., Li, Y.S., 2002. Analytical and experimental investigation on the hydrodynamic performance of onshore wave-power devices. Ocean. Eng. 29 (8), 871–885.
Wang, Z., Zou, Q., Reeve, D., 2009. Simulation of spilling breaking waves using a two phase flow cfd model. Comput. Fluids 38 (10), 1995–2005.
Wolgamot, H.A., Fitzgerald, C.J., 2015. Nonlinear hydrodynamic and real fluid effects on wave energy converters. Proc. Institution Mech. Eng. Part A J. Power Energy 1–23.
Zhang, Y., Zou, Q.-P., Greaves, D., 2012. Air–water two-phase flow modelling of hydrodynamic performance of an oscillating water column device. Renew. Energy 41, 159–170.
Zou, Q., Peng, Z., 2011. Evolution of wave shape over a low-crested structure. Coast. Eng. 58 (6), 478–488.
Zou, Q.P., 2004. A simple model for random wave bottom friction and dissipation. J. Phys. Oceanogr. 34 (6), 1459–1467.